

# Multifunctional microbubbles and nanobubbles for photoacoustic and ultrasound imaging

Chulhong Kim,<sup>a</sup> Ruogu Qin,<sup>b</sup> Jeff S. Xu,<sup>b</sup>  
Lihong V. Wang,<sup>a,\*</sup> and Ronald Xu<sup>b,†</sup>

<sup>a</sup>Washington University in St. Louis, Department of Biomedical Engineering, Optical Imaging Laboratory, One Brookings Drive, St. Louis, Missouri 63130

<sup>b</sup>The Ohio State University, Department of Biomedical Engineering, 270 Bevis Hall, 1080 Carmack Road, Columbus, Ohio 43210

**Abstract.** We develop a novel dual-modal contrast agent—encapsulated-ink poly(lactic-co-glycolic acid) (PLGA) microbubbles and nanobubbles—for photoacoustic and ultrasound imaging. Soft gelatin phantoms with embedded tumor simulators of encapsulated-ink PLGA microbubbles and nanobubbles in various concentrations are clearly shown in both photoacoustic and ultrasound images. In addition, using photoacoustic imaging, we successfully image the samples positioned below 1.8-cm-thick chicken breast tissues. Potentially, simultaneous photoacoustic and ultrasound imaging enhanced by encapsulated-dye PLGA microbubbles or nanobubbles can be a valuable tool for intraoperative assessment of tumor boundaries and therapeutic margins. © 2010 Society of Photo-Optical Instrumentation Engineers. [DOI: 10.1117/1.3302808]

Keywords: microbubbles; nanobubbles; photoacoustic imaging; ultrasound imaging; tumor margin intraoperative assessment.

Paper 09505LR received Nov. 13, 2009; revised manuscript received Jan. 1, 2010; accepted for publication Jan. 6, 2010; published online Feb. 18, 2010.

Surgical resection followed by radiation therapy and chemotherapy is the most effective treatment for malignant intracranial tumors.<sup>1,2</sup> Yet accurate localization of tumors and their boundaries is a critical issue with this method. Intraoperative magnetic resonance imaging (MRI) is currently the most reliable tool to identify the structural features of tumors. However, MRI alone is not sufficient to delineate diffuse tumor margins, because it cannot identify molecular characteristics at the cellular level.<sup>3,4</sup> Ultrasound (US) imaging has been applied as an alternative for tumor resection control, because this imaging modality is relatively inexpensive, portable, and fast enough to provide real-time images.<sup>5</sup> However, due to its low contrast, speckle artifacts, and high operator dependence, the reliability of US imaging is not fully proven.<sup>6</sup> Taking advantage of strong endogenous and exogenous opti-

cal contrasts, pure optical imaging has been intraoperatively applied to map tumor margins.<sup>7</sup> However, due to strong light scattering, pure optical imaging suffers from either shallow penetration depth (optical microscopy<sup>8</sup>) or poor spatial resolution (diffuse optical tomography<sup>9</sup>). Along with the application of new imaging techniques, contrast agents have been intensively investigated to improve the degree of resection and preserve normal tissues.<sup>10–12</sup> Therefore, there is a pressing need to develop a highly sensitive and high resolution imaging tool with proper contrast agents for monitoring surgical resection of intracranial tumors.

Thanks to its strong optical absorption contrast and high ultrasonic resolution, photoacoustic (PA) imaging has become a popular technique in tumor imaging *in vivo*.<sup>13</sup> The principle of this technique is that acoustic waves are generated through thermoelastic expansion when targets absorb a short-pulsed light.<sup>14,15</sup> The acoustic waves propagate in biological tissues and are detected by ultrasound transducers. The initial pressure rise is proportional to the local optical absorption (the product of the local optical absorption coefficient and the local optical fluence). The locations of optically absorptive targets can be measured using the arrival times of ultrasound. Since the spatial resolution at depths beyond one optical transport mean free path ( $> 1$  mm) is determined by acoustic parameters, the resolution and imaging depth can be scalable, while pixel numbers, defined as the ratio of the imaging depth to the resolution, are maintained at greater than 100. In addition, a conventional ultrasound system can be easily combined with PA imaging to provide both mechanical contrast (morphological information) and optical contrast (morphological and functional information).

In this work, for the first time to our knowledge, we have demonstrated a novel multifunctional contrast agent for PA and US imaging—encapsulated-ink poly(lactic-co-glycolic acid) (PLGA) microbubbles (MBs) and nanobubbles (NBs). We successfully imaged gelatin-based encapsulated-ink PLGA MBs and NBs at various concentrations using both PA and US imaging systems. Moreover, deeply positioned ( $\sim 1.8$  cm below biological tissues) encapsulated-ink PLGA MBs and NBs were clearly imaged using the PA imaging system. These results show that encapsulated-dye PLGA MBs and NBs can potentially be employed to assess intracranial tumor boundaries and therapeutic margins intraoperatively using simultaneous PA and US imaging.

Encapsulated-ink PLGA (50:50, RG 502H 12000 Da MW, Boehringer Ingelheim, Germany) MBs and NBs were fabricated using a modified double-emulsion process.<sup>16</sup> First, four solutions were prepared: 1. 5 mL of 2.5% w/v PLGA solution of methylene chloride ( $\text{CH}_2\text{Cl}_2$ , Fisher Scientific, Worcester, Massachusetts), 2. 50 mL of 4% w/v polyvinyl alcohol (PVA, Fisher Scientific) aqueous solution; 3. 0.5 mL of 50% v/v ink (Higgins Fountain Pen India nonwaterproof black ink, Sanford, Chicago, Illinois) and 4% w/v PVA aqueous solution; and 4. 100 mL of 5% v/v isopropanol aqueous solution. After that, the 0.5-mL aqueous solution of ink and PVA was added to the 5-mL PLGA solution of  $\text{CH}_2\text{Cl}_2$ , and emulsified in an ice bath. Then, the emulsion was added drop-wise using a 1000- $\mu\text{L}$  pipette to the 50-mL PVA solution in an ice bath and emulsified again. The double emulsion was then added to

\*Address all correspondence on photoacoustic imaging to: Lihong V. Wang, Washington University in St. Louis, Department of Biomedical Engineering, St. Louis, MO 63130. Tel: 314-935-6152; Fax: 314-935-7448. E-mail: lhwang@biomed.wustl.edu

†Address all correspondence on micro- and nanobubbles to: Ronald Xu, The Ohio State University, Department of Biomedical Engineering, Columbus, OH 43210. Tel: 614-688-3635; Fax: 614-292-7301. E-mail: xu.202@osu.edu

the isopropanol solution, stirred for 1.5 h by a magnetic stirrer, and then centrifuged. After centrifugation, the supernatant was discarded, and the bubble precipitate was washed by deionized water. The process of centrifugation and washing was repeated three times. The washed spheres were then freeze-dried by a Lyph-lock 4.5 freeze-dry system (Labconco Corporation, Kansas City, Missouri) for 36 h. Dried bubbles were harvested and stored in a glass bottle at 0 °C for further use. For the MBs, the first and second emulsion steps were conducted with a model 17105 Omni Mixer homogenizer (Omni International, Kennesaw, Georgia) at 20,000 rpm for 5 min and 10,000 rpm for 3 min, respectively. The centrifugation was carried out with a Centrifuge 5810R (Eppendorf, Hamburg, Germany) at 1500 rpm for 10 min. For the NBs, the first and second emulsion steps were conducted with an Omni-Ruptor 250 ultrasound probe (Omni International) at 90 W for 2 min and at 30 W for 1 min, respectively. The centrifugation was carried out with a Sorvall RC-5B high-speed centrifuge (Sorvall, Waltham, Massachusetts) at 9000 rpm for 10 min.

Eight cylindrical MB and NB tumor simulators, 5 mm in diameter, were fabricated by dispersing MBs and NBs respectively in gelatin solution at four different concentrations (2.5, 5, 10, and 15 mg/mL). The gelatin solution (concentration: 0.15 g/mL) was preheated by a microwave oven and degassed by a vacuum pump in advance. A tissue simulating phantom was fabricated by casting the cylindrical MB and NB tumor simulators in a gelatin pad of 3 × 4 × 0.5 cm.

The tissue simulating phantom was imaged by a 5-MHz linear array US probe (Terason, Burlington, Massachusetts) and a PA macroscope. The schematic of PA macroscope and the mechanisms of the ring-shaped light illumination are fully described in Ref. 17. To irradiate the phantoms, we used the wavelength-tunable Ti-sapphire laser (LT-2211A, Lotis TII, Minsk, Belarus), pumped by a Q-switched Nd:YAG laser (LS-2137, Lotis) with a pulse duration of 6.5 ns and a pulse repetition rate of 10 Hz. The light fluence on the phantom surface was 3.4 mJ/cm<sup>2</sup>, within the current ANSI limit.<sup>18</sup> A doughnut-shaped light ( $\lambda = 767$  nm), formed by concave and conical lenses, traveled through an optical condenser, and was coaxially focused with the ultrasound focal zone in water. The phantoms were positioned under a water tank that had a window with a transparent thin membrane. The PA waves, detected by a single-element 5-MHz ultrasound transducer (V308, Panametrics-NDT, Waltham, Massachusetts), were first amplified and then transferred to an oscilloscope. The axial and lateral resolutions were 138 and 490  $\mu\text{m}$ , respectively. One-dimensional depth-sensitive images along the  $z$  axis (referred to as A-lines) were obtained by measuring the times of arrival of the PA signals. By scanning the samples along the  $x$  and  $y$  directions, 3-D PA images were formed. 3-D images were projected into 2-D images through maximum amplitude projection (MAP), which projected the strongest signal along each A-line onto the corresponding  $x$ - $y$  plane.

A schematic of encapsulated-ink MBs and NBs is shown in Fig. 1(a). The volume-weighted size distributions, defined as the multiplication of the number distribution and the volume of particles, of MBs and NBs are plotted in Figs. 1(b) and 1(c), respectively. The average size of MBs is  $1.01 \pm 0.73 \mu\text{m}$ , and that of NBs is  $0.29 \pm 0.09 \mu\text{m}$ . Figures 2(a)–2(c) are photographic, PA, and US images acquired from

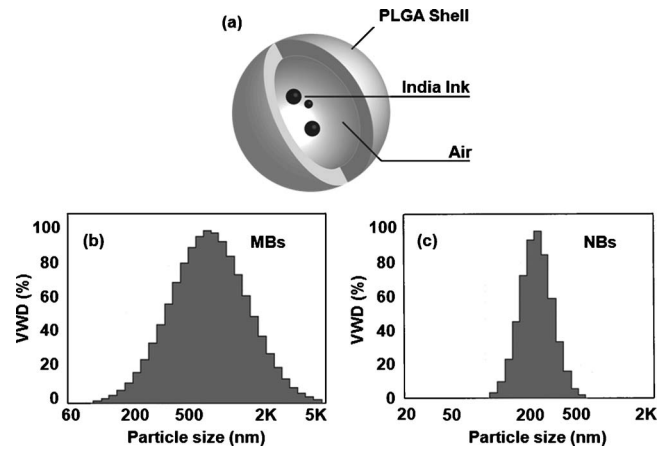


Fig. 1 (a) Schematic of MBs and NBs encapsulating black India ink. The size distributions of encapsulated-ink (b) MBs and (c) NBs. The x axis is a log scale. VWD: Volume weighted distribution.

the same gelatin phantom. Targets 1 through 4 are tumor simulators made of encapsulated-ink MBs at concentrations of 2.5, 5.0, 10, and 15 mg/mL, respectively. Targets 5 through 8 are tumor simulators composed of encapsulated-ink NBs at concentrations of 2.5, 5.0, 10, and 15 mg/mL, respectively. All eight targets are clearly shown in the PA images [Fig. 2(b)] and matched well with the photograph. In the corresponding US image [Fig. 2(c)], although targets 1 and 2 are not clearly shown, possibly owing to multiple factors including US depth of focus and/or low concentration of contrast agent, the other six targets are clearly visible. The PA signals are quantified as a function of concentration in Fig. 2(d). As the concentration mounts, the PA signals increase linearly. Since the average size of MBs was bigger than that of NBs, the MBs encapsulated more ink, and consequently PA signals

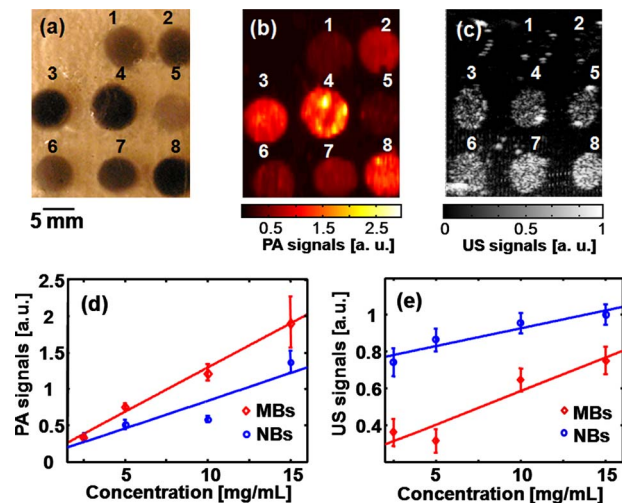
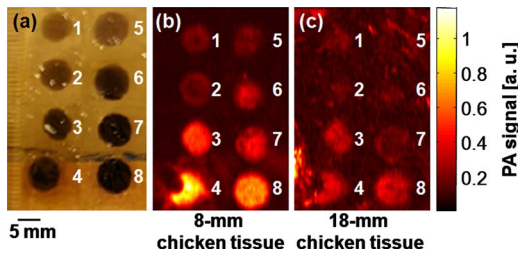


Fig. 2 (a) Photograph of a phantom containing tumor simulators made of encapsulated-ink MBs and NBs with various concentrations. (b) The corresponding PA image. (c) The corresponding US image. (d) The quantification of the PA signals at various concentrations of MBs and NBs. (e) The quantification of the US signals at various concentrations of MBs and NBs. 1 through 4: MBs at concentrations of 2.5, 5.0, 10, and 15 mg/mL, respectively. 5 through 8: NBs at concentrations of 2.5, 5.0, 10, and 15 mg/mL, respectively.



**Fig. 3** (a) Photograph of a phantom containing tumor simulators made of encapsulated-ink MBs and NBs with various concentrations. (b) The corresponding PA image of the phantom positioned below 8 mm of chicken breast tissues. (c) The corresponding PA image of the phantom positioned below 18 mm of chicken breast tissues. 1 through 4: MBs at concentrations of 2.5, 5.0, 10, and 15 mg/mL, respectively. 5 through 8: NBs at concentrations of 2.5, 5.0, 10, and 15 mg/mL, respectively.

from MBs were stronger than those from NBs. Figure 2(e) shows a linear increase of the US signals as a function of concentration. Note that the US signals in NBs are stronger than those in MBs. The enhanced acoustic contrast by NBs has not been well studied yet, possibly due to particle aggregation and the layering effect.<sup>19,20</sup> These results strongly support the dual functionality of encapsulated-ink MBs and NBs for PA and US imaging, where the optical contrast stems from ink and the mechanical contrast from bubbles.

To take advantage of the deeper penetration depth of PA imaging with high resolution, we added chicken breast tissues atop the phantom. The phantom was prepared in the same method as mentioned before [Fig. 3(a)]. With an 8-mm-thick layer of chicken breast tissue, all eight targets are clearly shown in Fig. 3(b). With an 18-mm-thick layer, although targets 1, 2, 5, and 6 are relatively dim, targets 3, 4, 7, and 8 are clearly visible in Fig. 3(c). This result implies that PA imaging is potentially able to delineate deep tumor margins using the encapsulated-ink MBs or NBs.

In summary, we successfully developed and tested encapsulated-ink PLGA MBs and NBs as a dual-modality contrast agent for PA and US imaging. Deeply positioned encapsulated-ink MBs and NBs were clearly imaged by the PA imaging. In the future, clinically practical organic dyes (such as indocyanine green) encapsulated in MBs and NBs can be tested in PA imaging.<sup>16</sup> By treating the surface of the bubbles to target specific molecules, the applications of these contrast agents using simultaneous PA and US imaging can be broadened to include not only intracranial tumor boundary mapping but also molecular imaging of primary and metastatic tumor.<sup>21</sup>

**Acknowledgments**

This work was supported in part by grants from the National Institutes of Health (R01 EB000712, R01 EB008085, R01 CA113453901, U54 CA136398—the Network for Translational Research, and 5P60 DK02057933 to Wang), and the Department of Defense Breast Cancer Research Program (W81XWH-07 to Xu). Wang has a financial interest in Micro-photoacoustics, Incorporated, and in Endra, Incorporated, which, however, did not support this work.

**References**

1. M. Ammirati, N. Vick, Y. L. Liao, I. Ciric, and M. Mikhael, "Effect of the extent of surgical resection on survival and quality of life in patients with supratentorial glioblastomas and anaplastic astrocytomas," *Neurosurgery* **21**(2), 201–206 (1987).
2. M. A. Hammoud, B. L. Ligon, R. elSouki, W. M. Shi, D. F. Schomer, and R. Sawaya, "Use of intraoperative ultrasound for localizing tumors and determining the extent of resection: a comparative study with magnetic resonance imaging," *J. Neurosurg.* **84**(5), 737–741 (1996).
3. P. C. Johnson, S. J. Hunt, and B. P. Drayer, "Human cerebral gliomas: correlation of postmortem MR imaging and neuropathologic findings," *Radiology* **170**(1), 211–217 (1989).
4. C. Nimsky, O. Gansland, M. Buchfelder, and R. Fahlbusch, "Intraoperative visualization for resection of gliomas: the role of functional neuronavigation and intraoperative 1.5 T MRI," *Neurol. Res.* **28**(5), 482–487 (2006).
5. G. Unsgaard, O. M. Rygh, T. Selbekk, T. B. Muller, F. Kolstad, F. Lindseth, and T. A. Hernes, "Intra-operative 3D ultrasound in neurosurgery," *Acta Neurochir.* **148**(3), 235–253 (2006).
6. M. Gerganov, A. Samii, A. Akbarian, L. Stueglitz, M. Samii, and R. Fahlbusch, "Reliability of intraoperative high-resolution 2D ultrasound as an alternative to high-field strength MR imaging for tumor resection control: a prospective comparative study," *J. Neurosurg.* **111**(3), 512–519 (2009).
7. R. Trehin, J. L. Figueiredo, M. J. Pittet, R. Weissleder, L. Josephson, and U. Mahmood, "Fluorescent nanoparticle uptake for brain tumor visualization," *Neoplasia* **8**(4), 302–311 (2006).
8. D. Huang, E. A. Swanson, C. P. Lin, J. S. Schuman, W. G. Stinson, W. Chang, M. R. Hee, T. Flotte, K. Gregory, C. P. Puliafito, and J. G. Fujimoto, "Optical coherence tomography," *Science* **254**(5035), 1178–1181 (1991).
9. B. W. Zeff, B. R. White, H. Dehghani, B. L. Schlaggar, and J. P. Culver, "Retinotopic mapping of adult human visual cortex with high-density diffuse optical tomography," *Proc. Natl. Acad. Sci. U.S.A.* **104**(29), 12169–12174 (2007).
10. M. M. Haglund, M. S. Berger, and D. W. Hochman, "Enhanced optical imaging of human gliomas and tumor margins," *Neurosurgery* **38**(2), 308–317 (1996).
11. M. M. Haglund, D. W. Hochman, A. M. Spence, and M. S. Berger, "Enhanced optical imaging of rat gliomas and tumor margins," *Neurosurgery* **35**(5), 930–940 (1994).
12. M. F. Kircher, U. Mahmood, R. S. King, R. Weissleder, and L. Josephson, "A multimodal nanoparticle for preoperative magnetic resonance imaging and intraoperative optical brain tumor delineation," *Cancer Res.* **63**(23), 8122–8125 (2003).
13. L. V. Wang, "Multiscale photoacoustic microscopy and computed tomography," *Nature Photon.* **3**(9), 503–509 (2009).
14. A. Rosencwaig and A. Gersho, "Theory of the photoacoustic effect with solids," *J. Appl. Phys.* **47**(1), 64–69 (1976).
15. M. Xu and L. V. Wang, "Photoacoustic imaging in biomedicine," *Rev. Sci. Instrum.* **77**(4), 041101 1–22 (2006).
16. R. Xu, J. Huang, J. Xu, D. Sun, G. Hinkle, J. Edward, W. Martin, and S. Pivoski, "Fabrication of indocyanine green encapsulated biodegradable microbubbles for structural and functional imaging of cancer," *J. Biomed. Opt.* **14**(3), 034020 (2009).
17. K. H. Song and L. V. Wang, "Deep reflection-mode photoacoustic imaging of biological tissue," *J. Biomed. Opt.* **2**(6), 060503 (2007).
18. American National Standard for Safe Use of Lasers (ANSI Z136.1–2000), Laser Institute of America, Orlando, FL (2000).
19. J. Liu, J. Li, T. J. Rosol, X. Pan, and J. L. Voorhees, "Biodegradable nanoparticles for targeted ultrasound imaging of breast cancer cells *in vitro*," *Phys. Med. Biol.* **52**(16), 4739–4747 (2007).
20. J. N. Marsh, K. C. Partlow, D. R. Abendschein, M. J. Scott, G. M. Lanza, and S. A. Wickline, "Molecular imaging with targeted perfluorocarbon nanoparticles: quantification of the concentration dependence of contrast enhancement for binding to sparse cellular epitopes," *Ultrasound Med. Biol.* **33**(6), 950–958 (2007).
21. J. S. Xu, J. Huang, R. Qin, G. Hinkle, S. Pivoski, E. Martin, and R. X. Xu, "Synthesizing and binding dual-mode poly (lactic-co-glycolic acid) (PLGA) nanobubbles for cancer targeting and imaging," *Bio-materials* **31**(7), 1716–1722 (2010).